Laser and Particle Beams (2011), *29*, 105–111.

doi:10.1017/S0263034611000048

Nucleation and growth of nanoparticles during pulsed laser deposition in an ambient gas

Y.L. WANG, C. CHEN, X.C. DING, L.Z. CHU, Z.C. DENG, W.H. LIANG, J.Z CHEN, AND G.S. FU
College of Physics Science and Technology, Hebei University, Baoding, China

(RECEIVED 18 October 2010; ACCEPTED 3 January 2011)

Abstract

We present a method to determine where the nanoparticles nucleate and grow during pulsed laser deposition in an ambient gas. Briefly, nanocrystalline Si films are systemically deposited on the substrates located at a distance from the plasma and placed in horizontal direction; meanwhile an external electric field is introduced perpendicularly to the plume. Based on the transportation dynamics of Si nanoparticles corresponding to different electric fields, the lateral nucleation range of 0.1 to 33.8 mm is determined for Si nanoparticles deposited in 10 Pa Ar gas at a laser fluence of 4 J/cm^2. Further simulation of the mass and area density of Si nanoparticles demonstrates that both nucleation and growth probabilities in nucleation region are approximately Gauss-dependent of the lateral distance.

Keywords: Nanoparticle; Nanoscale structure; Nucleation and growth; Nucleation region; Pulsed laser deposition

1. INTRODUCTION

Intense laser beam interaction with solid surface has been investigated for many years, but it is still an attractive field (Chen *et al.*, 2009; Liu *et al.*, 2010; Okamuro *et al.*, 2010; Wang *et al.*, 2010) because more and more novel phenomena are discovered. It is used in processing of materials *via* pulsed laser ablation and has wide spread applications in such as particle beam generation (Bin *et al.*, 2009), medical therapy (Linz & Alonso, 2007; Yogo *et al.*, 2009), laser-induced nuclear reactions (Renner *et al.*, 2008; Torrisi *et al.*, 2008), diagnostics for laser-plasma interaction (MacKinnon *et al.*, 2004), laser-driven ion accelerators (Badziak *et al.*, 2001; Krushelnick *et al.*, 2007; Malka *et al.*, 2008; Mangles *et al.*, 2006), proton radiography and imaging (Borghesi *et al.*, 2002; Breschi *et al.*, 2004; Cobble *et al.*, 2002), fast ignition in inertial confinement fusion (Roth *et al.*, 2001), and thin film deposition (Caridi *et al.*, 2008; Wang *et al.*, 2007). For the preparation of thin film containing nanoscale structures (e.g., nanoparticles, nanowires, nanotubes) by using ns-pulsed laser deposition (PLD), a high-energy laser beam focused on a target induces the heating, melting, evaporation of a thin layer of the irradiated material (Aghaei *et al.*, 2008), and thus the formation of plasma associated with the production of particle emission in front of the target (Alti & Khare, 2006; Trusso *et al.*, 2005; Wang *et al.*, 2009). The charged ions with energies between tens and hundreds of eV (Schmid *et al.*, 2009) collide with ambient gas, and produce the charged nanoscale structures by the condensation process (Hirasawa *et al.*, 2006; Muramoto *et al.*, 1999; Seto *et al.*, 2001, 2003), and finally are deposited on the substrate to form the thin film.

Although PLD has been used to fabricate nanoscale structures for more than 10 years (Umezu *et al.*, 2008; Werwa *et al.*, 1994), it is still difficult to carry out the controllable preparation as we expect. Only when the formation dynamics is clarified, can we obtain the nanoscale structures we want. Numerous earnest efforts have been made to understand the formation dynamics, but some basic, yet significant problems are not entirely clear. For a typical example, in what quantitative conditions can the nanoscale structures form? Thus, where and how do the nanoscale structures form? As already known, during the formation of nanoscale structures, nucleation and growth are always two crucial processes that we can not parry (Morales & Lieber 1998; Yan *et al.*, 2009). Morales and Lieber (1998) skillfully prepared Si and Ge nanowires by vapor-liquid-solid growth on the basis of pulsed laser ablation nucleation in a quartz tube. Their nanowire formation model revealed that the nucleation occurs due to hot vapor condensation as the ablated species cool through collisions with the background gas, and the growth begins when the temperature and Si/Ge density get to their critical values and maintains until these conditions

Address correspondence and reprint requests to: Ying-Long Wang, College of Physics Science and Technology, Hebei University, Baoding 071002, China. E-mail: hdwangyl@mail.hbu.edu.cn

cannot be met. This idea can be extended to the nucleation and growth of nanoscale structures with other configurations in various preparation methods. To explain the experimental result that Ne gas induces the smallest and most uniform Si nanoparticles (np-Sis, i.e., Si nanograins, nanocrystals, nanoclusters or quantum dots) among He, Ar, and Ne, we proposed a qualitative model (Fu *et al.*, 2005), which indicated that for ns-PLD, there are three regions, labeled "high energy region," "nucleation region" (NR), and "transporting region." The mean size and size-consistency of np-Sis depend on the width of NR where the nucleation and growth occur. With the modification that the metal atoms can bond with the background gas, our model was extended to organometallic complexes formation by laser ablating transition metals in ethylene (Phillips & Shivaram, 2009). Obviously, the determination of the NR during PLD is very helpful to quantitative clarification of the formation conditions for nanoscale structures. As a model material, the nucleation location and growth process of np-Si are investigated in this article due to its unique properties, e.g., light emission by quantum confinement, single electron transport such as Coulomb blockade and photonic band gap crystals.

2. EXPERIMENTAL DETAILS

The discussed NR is in the one-dimensional range in the axial direction. To study the information on the location of np-Si nucleation and growth, we placed the deposition substrates under the plasma and in horizontal direction (Fig. 1), which is different from the conventional PLD setup. This design, moreover, can avoid the influence of the substrate in conventional PLD system on the NR due to the oscillation of mixed region (Wang *et al.*, 2006). Although the formed np-Si moves as a simple horizontal projectile motion from the NR to the substrate, we can not ascertained NR by PLD dynamics calculation based on the experimental data about the np-Sis without the slowing coefficient and the initial velocity of ablated particles (Yoshida *et al.*, 1996).

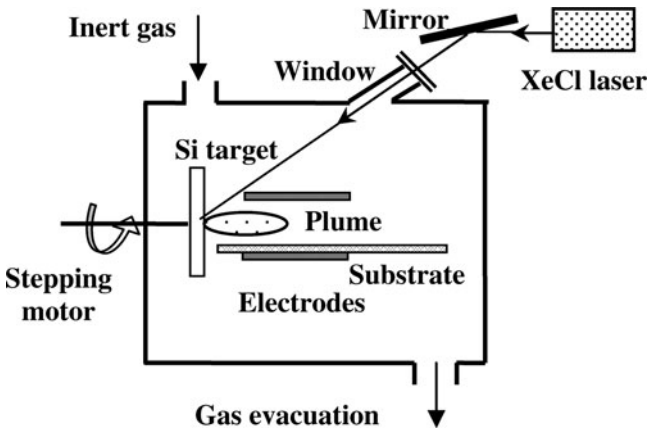

Fig. 1. The schematic diagram of the experiment used to determine the nucleation region in pulsed laser ablation.

Noted that the simultaneous determination of the NR location and these unknown parameters needs three dynamics equations, an external electric field is introduced perpendicularly to the plume (Fig. 1). The introduced field with appropriate direction can make np-Sis get to substrates more quickly because np-Sis are positively charged (Muramoto *et al.*, 1999; Seto *et al.*, 2001, 2003; Hirasawa *et al.*, 2006). Three electric fields for various voltages can induce three PLD dynamics equations, from which the location of

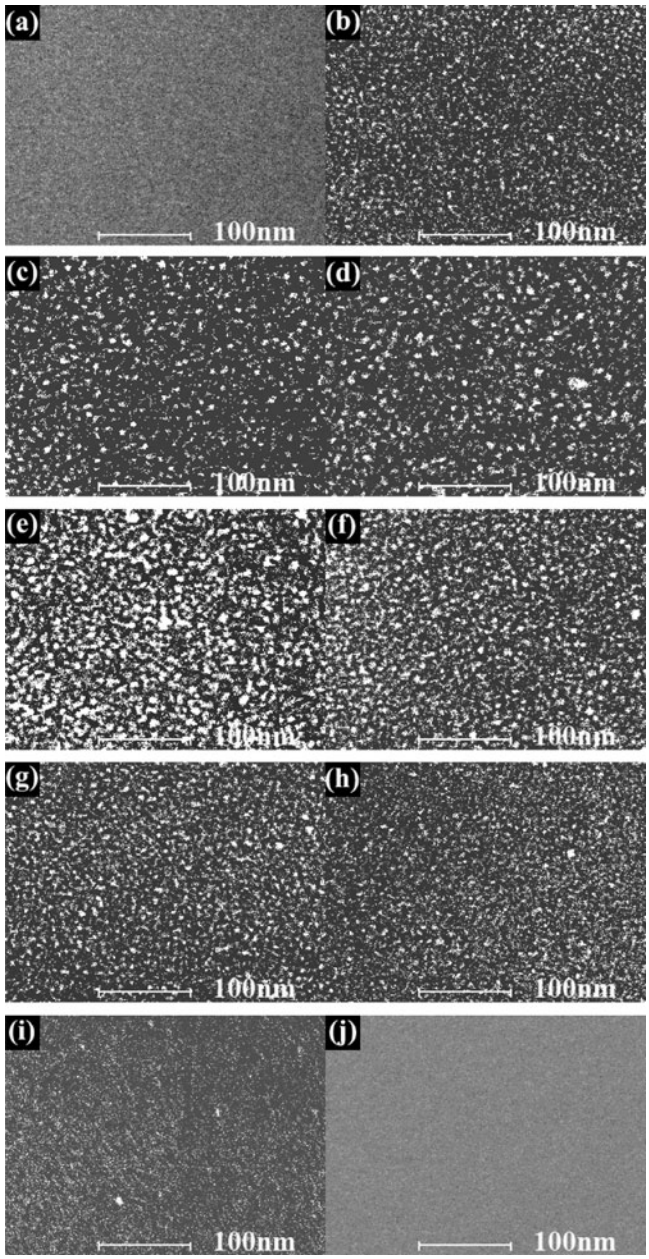

Fig. 2. SEM images of the Si films deposited by pulsed laser ablation in 10 Pa Ar gas under the dc voltage of 50 V. Where (**a**), (**b**), (**c**), (**d**), (**e**), (**f**), (**g**), (**h**), (**i**), and (**j**) correspond to the various lateral distance from Si target of 4.5 mm, 5 mm, 10 mm, 15 mm, 20 mm, 25 mm, 30 mm, 35 mm, 36.1 mm, and 36.5 mm, respectively.

https://doi.org/10.1017/S0263034611000048 Published online by Cambridge University Press

NR, the slowing coefficient, and the initial velocity can be determined.

In our PLD apparatus (Fig. 1), Lambda Physik XeCl excimer laser (wavelength 308 nm, laser fluence 4 J/cm^2, pulse duration 15 ns, repetition rate 1 Hz) was used. The resistivity of single crystalline Si target was 3000 Ω·cm. An electric field was applied by a direct current voltage between parallel aluminum electrodes placed perpendicularly to the target surface. The distance between the electrodes was 40 mm, and they were positioned from 1 to 55 mm at the right of the target surface. Different voltages of 50 V, 100 V, and 200 V were applied to the two electrodes. A series of single crystalline (111) Si or glass slices substrates were placed on the bottom electrode. Ar gas in a vacuum chamber was kept at a constant pressure of 10 Pa. The typical deposition time was 10 min. Scanning electron microscopy (SEM; FEI Sirion XL30), Raman (MKI-2000), and X-ray diffraction (XRD; Rigaku D/Max) were employed to characterize the microstructural properties of the films.

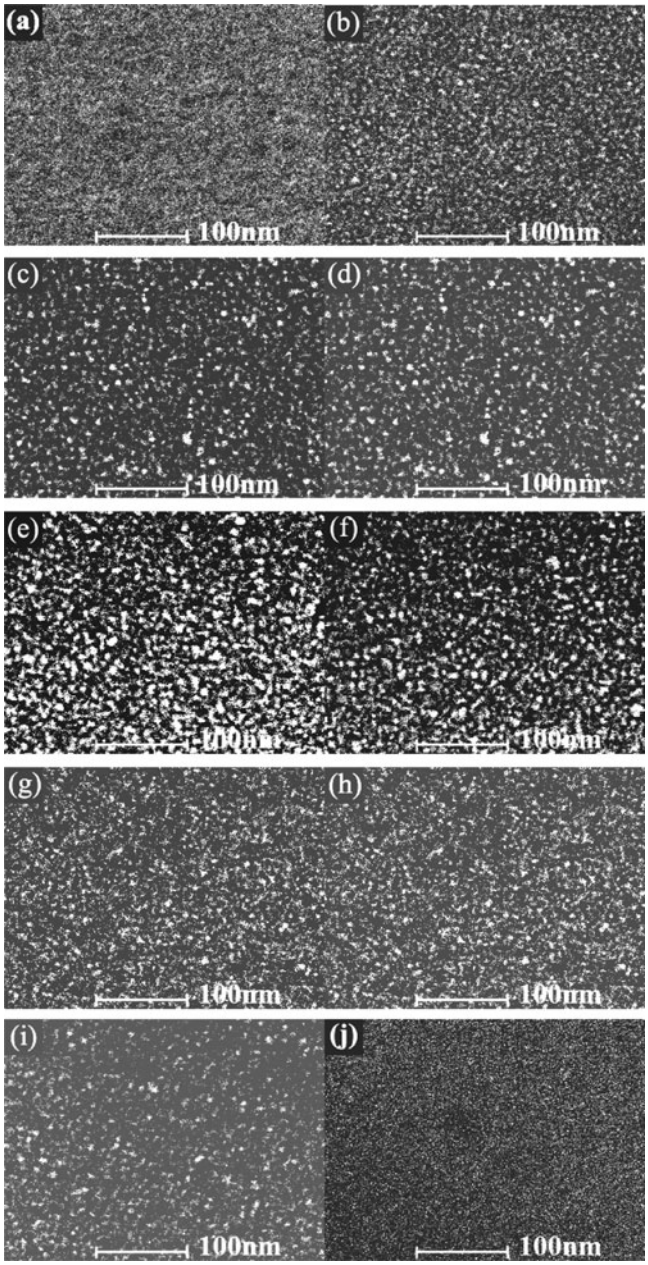

Fig. 3. SEM images of the Si films deposited by pulsed laser ablation in 10 Pa Ar gas under the dc voltage of 100 V. Where (**a**), (**b**), (**c**), (**d**), (**e**), (**f**), (**g**), (**h**), (**i**), and (**j**) correspond to the various lateral distance from Si target of 3 mm, 3.6 mm, 8.5 mm, 13.5 mm, 18.5 mm, 23.5 mm, 28.5 mm, 33.5 mm, 35.5 mm, and 36 mm, respectively.

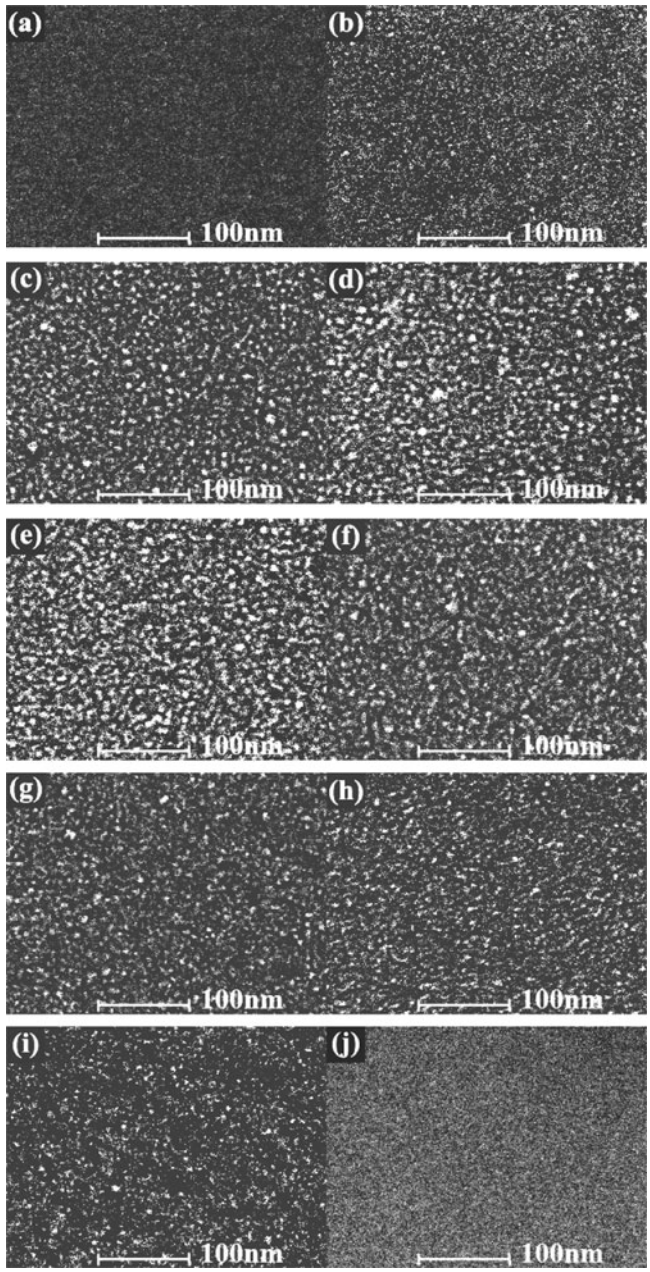

Fig. 4. SEM images of the Si films deposited by pulsed laser ablation in 10 Pa Ar gas under the dc voltage of 200 V. Where (**a**), (**b**), (**c**), (**d**), (**e**), (**f**), (**g**), (**h**), (**i**), and (**j**) correspond to the various lateral distance from Si target of 2 mm, 2.5 mm, 7.5 mm, 12.5 mm, 17.5 mm, 22.5 mm, 27.5 mm, 32.5 mm, 34.9 mm, and 35.3 mm, respectively.

https://doi.org/10.1017/S0263034611000048 Published online by Cambridge University Press

The SEM images of the films prepared under 50 V, 100 V, and 200 V for the typical lateral distances from Si target are shown in Figures 2, 3, and 4, respectively. In Figure 2a–2j correspond to the various lateral distances of 4.5 mm, 5 mm, 10 mm, 15 mm, 20 mm, 25 mm, 30 mm, 35 mm, 36.1 mm, and 36.5 mm, respectively. Obviously, no np-Sis can be seen in Figures 2a and 2j, all the films located at 5–36.1 mm contain np-Sis, that is to say, 5 mm and 36.1 mm are, respectively, the distance that np-Sis appear (starting distance) and the distance that np-Sis disappear (ending distance) on the substrate. Figures 3 and 4 shows that the starting-ending distances on the substrate are, respectively, 3.6–35.5 mm and 2.5–34.9 mm for 100 V and 200 V. It is obvious that 100 V and 200 V induce the smaller starting and ending distances than 50 V. The mean size and area density of np-Sis in the films located at various lateral distances can be obtained from statistic operation, as the squares for 50 V, the circles for 100 V and the uptriangles for 200 V are shown in Figure 5a and 5b, respectively. Obviously, both the mean size and area density of np-Sis first increase to a maximum at about 20 mm and then decreases with the increase of lateral distance. The corresponding Raman spectra of the films prepared under 50 V are demonstrated in Figure 6a, in which the peaks in the vicinity of 520 cm^{-1} indicate that the grains appearing in Figures 2b–2i are nanocrystalline. Additionally, with increasing lateral distance, the Raman peaks first right-shift and then left-shift, implying that the grain size varies as indicated in SEM images, which can be further confirmed by the width variation of (111) crystalline peaks in Figure 6b, XRD spectra

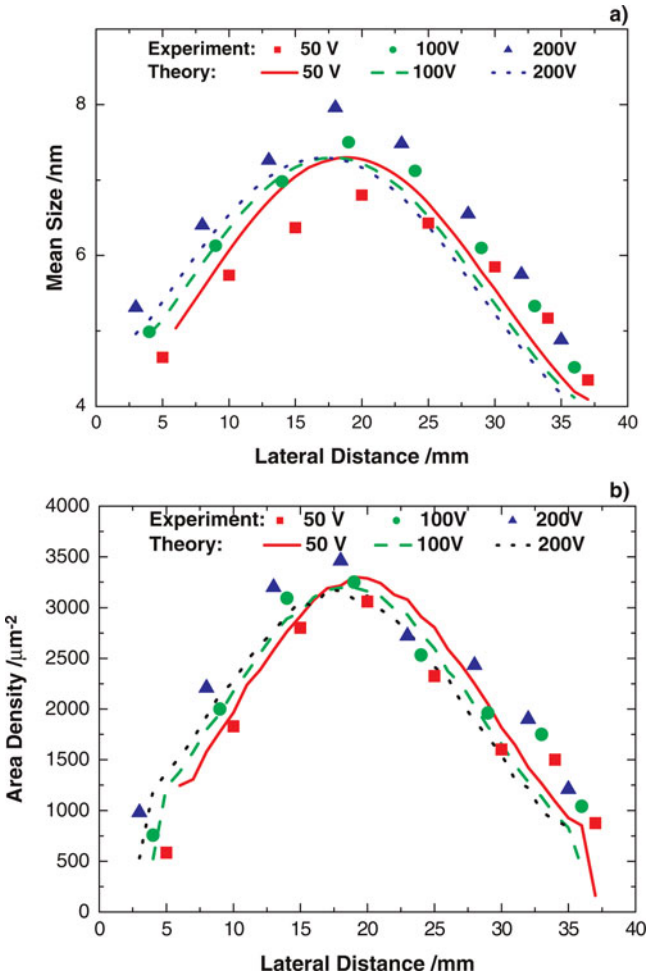

Fig. 5. (Color online) The experimental data (symbols) and theoretical results (curves) about the mean size (**a**) and area density (**b**) of Si nanoparticles in the films located at various lateral distances. The squares, the circles, uptriangles correspond to the experimental results for 50 V, 100 V, and 200 V, respectively. The solid, dashed and dotted curves correspond to the theoretical results for 50 V, 100 V, and 200 V, respectively.

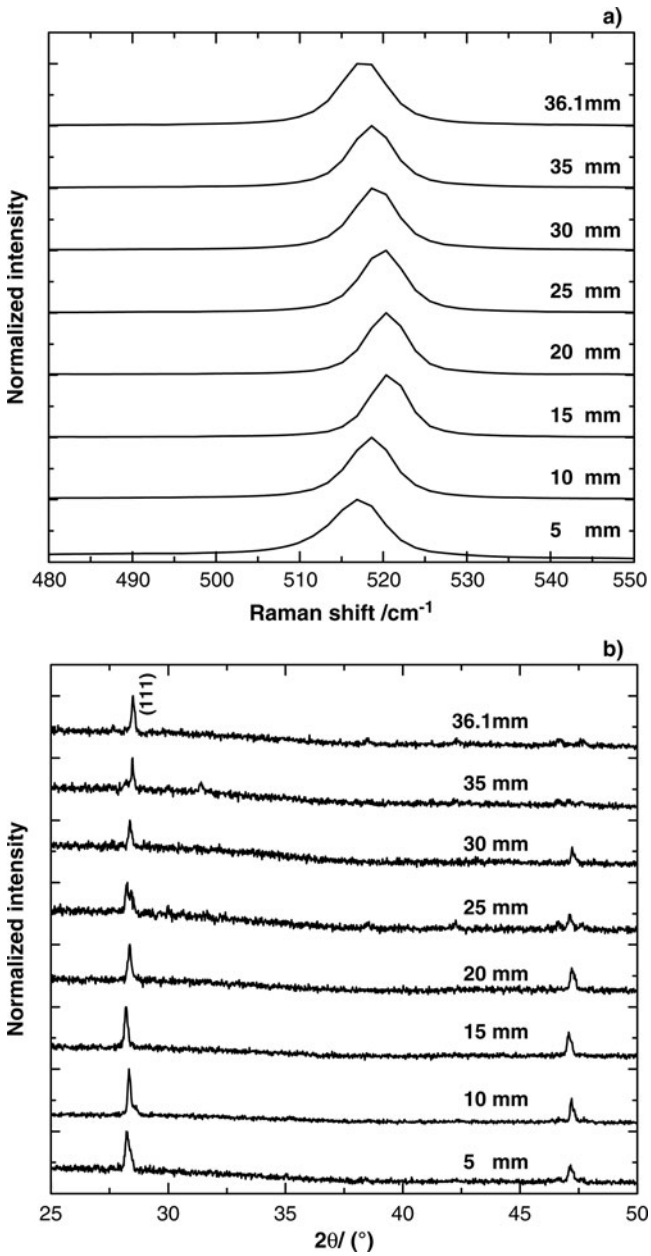

Fig. 6. The Raman spectrum (**a**) and XRD spectrum (**b**) of Si films deposited by pulsed laser ablation in 10 Pa Ar gas under the direct current voltage of 50 V.

https://doi.org/10.1017/S0263034611000048 Published online by Cambridge University Press

of the films under 50 V. It should be emphasized that the observed lateral dependence of nanoparticle deposition can be used for the size selection of nanoparticles.

3. THEORETICAL MODEL AND CALCULATION

Figure 7 demonstrates the formation and propagation of np-Sis. The ablated particles (Si atoms and so on) with the initial velocity of $v_{0\mathrm{Si}}$ are ejected from the surface of the Si target when the pulsed laser ablates Si target and they gradually release their kinetic energy (corresponding velocity v_{Si}) by colliding with ambient atoms. Most ablated particles are distributed in plume where the axis located at h (20 mm) from the substrate, and they are agglomerated to form np-Sis with velocity of v_Δ at x_0 in NR. Because the NR is above the substrates, the np-Sis formed in NR is deposited on the substrates after undergoing "horizontal projectile motion" under gravity. It is believed that the formed np-Sis are positively charged, here the electric quantity $q = +e$ is assumed (Seto *et al.*, 2003), in which e is the electrical elementary charge. Thus, when the electric field $E = U/(2h)$ is applied, the motion of np-Sis in the field is horizontal projectile-like, where U denotes the voltage between the two electrodes. The calculation shows that compared with the electric field force, gravity can be ignored in our work. It is natural that 100 V induces the smaller starting and ending distance than 50 V and the smallest starting and ending distances take place at 200 V. According to the inertia fluid model proposed by Yoshida *et al.* (1999), $v_{\mathrm{Si}} = v_{0\mathrm{Si}}\exp(-\alpha x_0/m_{\mathrm{Si}})$, in which m_{Si} is the mass of Si atom and $\alpha = BS\rho/2$ is the slowing coefficient, B is the proportional constant, $S = \pi(r_{\mathrm{Si}} + r_{\mathrm{Ar}})^2$ is the cross-section, and ρ denotes the ambient gas density. It is supposed that $m_\Delta {v_\Delta}^2/2 = C^2(m_{\mathrm{Si}}{v_{\mathrm{Si}}}^2)/2$ and $m_{\mathrm{Si}}/m_\Delta = (r_{\mathrm{Si}}/r_\Delta)^3$, where C is the energy transformation coefficient, m_Δ is the mass of the nanoparticles, r_{Si} and r_Δ are the radii of the Si atom, and the formed np-Si, respectively. In the horizontal direction, the formed np-Sis at x_0 are exerted a resistance by the ambient, with a similar form to Si atom except for the cross-section of $\pi(r_\Delta + r_{\mathrm{Ar}})^2$. Based on the dynamic equation of horizontal projectile in the electric field E, the position x of np-Si deposited on the substrate can be obtained by

$$x = x_0 + Cv_{0Si}\exp\left[-\frac{\alpha\, x_0}{m_{Si}}\right]\exp \times\left[-\frac{\alpha\,(x-x_0)}{m_{Si}}\left(\frac{r_\Delta + r_{Ar}}{r_{Si}+r_{Ar}}\right)^2\left(\frac{r_{Si}}{r_\Delta}\right)^3\right]\sqrt{\frac{2hm_{\mathrm{Si}}}{qE}}. \quad (1)$$

For np-Si, when x (the distance on the substrate) is measured, the corresponding x_0 (the distance in the NR) can be determined by Eq. (1). From $m_\Delta {v_\Delta}^2/2 = C^2(m_{\mathrm{Si}}{v_{\mathrm{Si}}}^2)/2$, np-Si with small size can obtain big horizontal velocity, thus it is reasonable that the np-Sis at ending position on the substrate are from the ending position of NR. Because the staring position on the substrate is quite near to the Si target, we think that this position corresponds to the staring position in NR. Namely, according to the staring and ending positions on the substrate obtained in the experiment, we can gain the staring and ending positions of NR based on Eq. (1). From Figure 5a, we know the ending positions on the substrate are, respectively, 36.1 mm, 35.5 mm, and 34.9 mm, and the size r_Δ of np-Si are, respectively, 4.35 nm, 4.52 nm, and 4.88 nm, for 50 V, 100 V, and 200 V, which determines the ending position of NR is 33.8 mm, and the parameters $\alpha = 1.09\times10^{-24}$ kg/m, $Cv_{0\mathrm{Si}} = 1641$ m/s. Similarly, the starting position of the NR is calculated as 0.1 mm with the same parameters α and $Cv_{0\mathrm{Si}}$. In our calculation, $m_{\mathrm{Si}} = 4.67\times10^{-26}$ kg, $r_{\mathrm{Si}} = 1.46$ Å and $r_{\mathrm{Ar}} = 0.88$ Å are used. In a word, the ablation with laser pulses of 4 J/cm^2 in 10 Pa Ar gas can form a NR ranging from 0.1 mm to 33.8 mm.

In NR from 0.1 mm to 33.8 mm, the mass m_Δ of np-Si formed at various position x can be supposed as

$$m_\Delta = m_{\Delta m}\exp\left[-\left(\frac{x-x_1}{w_1}\right)^2\right], \quad (2)$$

which indicates that the size of the formed np-Si first increases to a maximum $m_{\Delta m}$ at x_1 and then decreases with increasing x, where w_1 decides the mass-changing rate. Similarly, the number N_Δ of np-Si formed at various position x can be given as

$$N_\Delta = N_{\Delta m}\exp\left[-\left(\frac{x-x_2}{w_2}\right)^2\right], \quad (3)$$

which reflects the nucleation probability of Si particles in the gas phase. Incorporated with Eq. (1), the mean size and area density of np-Sis on the substrate at various lateral distances, appended in Figure 5, are obtained by numerical simulation and statistic calculation. The solid, dashed, and dotted curves in Figures 5a and 5b, respectively, correspond to the results for 50 V, 100 V, and 200 V. Obviously, the theoretical results perfectly depict the varying behavior found in the

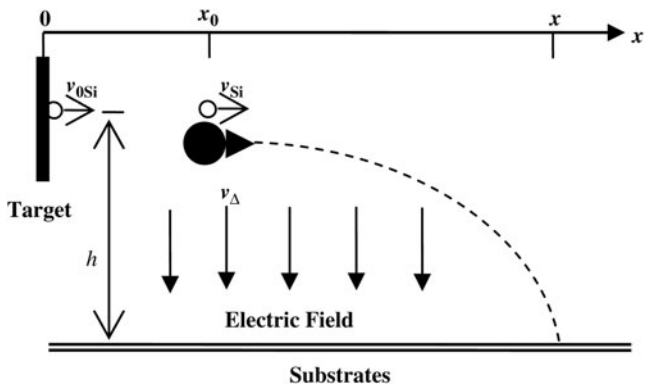

Fig. 7. The schematic diagram for the formation and propagation of Si nanoparticles.

https://doi.org/10.1017/S0263034611000048 Published online by Cambridge University Press

experiment. More importantly, some crucial quantities in Eqs. (2) and (3) are obtained in the simulation, i.e., $m_{\Delta m} = 10060m_{\mathrm{Si}}$, $x_1 = 14.9$ mm, $w_1 = 13.4$ mm, $N_{\Delta m} = 1510$, $x_2 = 15.8$ mm, $w_2 = 14.7$ mm, which quantitatively gives some pictures on the NR: The ejected Si atoms cannot gather into nanoparticle before $x = 0.1$ mm. 498 nanoparticles with mass of $3176m_{\mathrm{Si}}$ (size of ~4.9 nm obtained by the first-principle calculation) are produced while the nucleation conditions are satisfied in the starting position of NR. With the increase of the axial distance from Si target, more np-Sis are formed, the number of Si nanoparticles increases to a maximum 1510 at 15.8 mm and then gradually decreases to 330 at the ending position of nucleation. The mass or size of the formed np-Si versus the axial distance possesses the similar varying tendency except for the peak position of 14.9 mm. The mass of np-Sis in the peak location and the ending position is $10060m_{\mathrm{Si}}$ (~7.3 nm) and $1790m_{\mathrm{Si}}$ (~4 nm), respectively.

4. CONCLUSIONS

A picture on the formation dynamics of nanoscale structures (e.g., nanoparticles) with the size and configuration we expect is very important to a controllable preparation method. Especially, it is crucial to quantitatively depict the nucleation location and growth process during nanoscale structure preparation. In this article, the location of nucleation region for Si nanoparticles formed during pulsed laser ablation in an ambient gas was determined based on the transportation dynamics at different electric fields corresponding to 50 V, 100 V, and 200 V through a special setup of the substrate parallel and applied electric field perpendicular to the plume. In the typical deposition conditions (laser fluence 4 $\mathrm{J/cm^2}$, ambient Ar pressure 10 Pa), the nucleation region locates at (0.1 mm, 33.8 mm) away from Si target. Further theoretical simulation for the mass and area density of Si nanoparticles on the substrate indicates that both nucleation and growth probabilities in the nucleation region are approximately Gauss-dependent of the lateral distance. This may pave a way for effectively determining the nucleation region and thus investigating the nucleation conditions for nanoparticles of Si as well as other materials formed in gas phase.

In many previous publications, the location of nucleation region for Si nanoparticles induced by a single-pulse was determined mainly by using charge-coupled device (CCD) techniques (Muramoto *et al.*, 2000; Nakata *et al.*, 2002). According to our previous work (Wang *et al.*, 2007), for the repetition rate of 1 Hz, the ambient restoration is nearly finished before the subsequent pulse ablates Si target, the dynamic process corresponding to the latter pulse is hardly affected by the background remained by the former pulse. Thus SEM images obtained in this experiment can be thought to be from the superposition effect of the multi-pulses. In this meaning, CCD result has the same order of magnitude with our data. The difference may be from the limit of time-response and resolving power of CCD.

The detailed nucleation and growth process, including the nucleation conditions of vapor density and velocity in the nucleation region, are complicate so that the further discussion is expected in the future work.

ACKNOWLEDGMENTS

The authors thank Professors B. T. Liu and Q. X. Zhao for the useful discussion. This work was supported by the NSFC (10774036), the NSF of Hebei Province (E2008000631) and foundation of Hebei University. The anonymous referee's critical suggestions are acknowledged.

REFERENCES

Aghaei, M., Mehrabian, S. & Tavassoli, S.H. (2008). Simulation of nanosecond pulsed laser ablation of copper samples: A focus on laser induced plasma radiation. *J. Appl. Phys.* **104**, 053303.

Alti, K. & Khare, A. (2006). Low-energy low-divergence pulsed indium atomic beam by laser ablation. *Laser Part. Beams* **24**, 47–53.

Badziak, J., Woryna, E., Parys, P., Platonov, K.Y., Jabłonski, S., Ryc, L., Vankov, A.B. & Wołowski, J. (2001). Fast proton generation from ultrashort laser pulse interaction with double-layer foil targets. *Phys. Rev. Lett.* **87**, 215001.

Bin, J.H., Lei, A.L., Yang, X.Q., Huang, L.G., Yu, M.Y., Yu, W. & Tanaka, K.A. (2009). Quasi-monoenergetic proton beam generation from a double-layer solid target using an intense circularly polarized laser. *Laser Part. Beams* **27**, 485–490.

Borghesi, M., Campbell, D.H., Schiavi, A., Willi, O., Mackinnon, A.J., Hicks, D., Patel, P., Gizzi, L.A., Galimberti, M. & Clarke, R.J. (2002). Laser-produced protons and their application as a particle probe. *Laser Part. Beams* **20**, 269–275.

Breschi, E., Borghesi, M., Campbell, D.H., Galimberti, M., Giulietti, D., Gizzi, L.A., Romagnani, L., Schiavi, A. & Willi, O. (2004). Spectral and angular characterization of laser-produced proton beams from dosimetric measurements. *Laser Part. Beams* **22**, 393–397.

Caridi, F., Torrisi, L., Margarone, D. & Borrielli, A. (2008). Investigations on low temperature laser-generated plasma. *Laser Part. Beams* **26**, 265–271.

Chen, H., Wilks, S.C., Bonlie, J.D., Liang, E.P., Myatt, J., Price, D.F., Meyerhofer, D.D. & Beiersdorfer, P. (2009). Relativistic positron creation using ultraintense short pulse lasers. *Phys. Rev. Lett.* **102**, 105001.

Cobble, J.A., Johnson, R.P., Cowan, T.E., Renard-Legalloudec, N. & Allen, M. (2002). High resolution laser-driven proton radiography. *J. Appl. Phys.* **92**, 1775–1779.

Fu, G.S., Wang, Y.L., Chu, L.Z., Zhou, Y., Yu, W., Han, L. & Peng, Y.C. (2005). The size distribution of Si nanoparticles prepared by pulsed-laser ablation in pure He, Ar or Ne gas. *Europhys. Lett.* **69**, 758–762.

Hirasawa, M., Orii, T. & Seto, T. (2006). Size-dependent crystallization of Si nanoparticles. *Appl. Phys. Lett.* **88**, 093119.

Krushelnick, K., Najmudin, Z. & Dangor, A.E. (2007). Particle acceleration using intense laser produced plasmas. *Laser Phys. Lett.* **4**, 847–862.

Linz, U. & Alonso, J. (2007). What will it take for laser driven proton accelerations to be applied to tumor therapy. *Phys. Rev. ST AB* **10**, 094801.

Liu, B., Zhang, H., Fu, L.B., Gu, Y.Q., Zhang, B.H., Liu, M.P., Xie, B.S., Liu, J. & He, X.T. (2010). Ion jet generation in the ultraintense laser interactions with rear-side concave target. *Laser Part. Beams* **28**, 351–359.

Mackinnon, A.J., Patel, P.K., Town, R.P., Edwards, M.J., Phillips, T., Lerner, S.C., Price, D.W., Hicks, D., Key, M.H., Hatchett, S., Wilks, S.C., Borghesi, M., Romagnani, L., Kar, S., Toncian, T., Pretzler, G., Willi, O., Koenig, M., Martinolli, E., Lepape, S., Benuzzi-Mounaix, A., Audebert, P., Gauthier, J.C., King, J., Snavely, R., Freeman, R.R. & Boehlly, T. (2004). Proton radiography as an electromagnetic field and density perturbation diagnostic. *Rev. Sci. Instrum.* **75**, 3531.

Malka, V., Faure, J., Gauduel, Y.A., Lefebvre, E., Rousse, A. & Phuoc, K.T. (2008). Principles and applications of compact laser-plasma accelerators. *Nat. Phys.* **4**, 447–453.

Mangles, S.P.D., Walton, B.R., Najmudin, Z., Dangor, A.E., Krushelnick, K., Malka, V., Manclossi, M., Lopes, N., Carias, C., Mendes, G. & Dorchies, F. (2006). Table-top laser plasma acceleration as an electron radiography source. *Laser Part. Beams* **24**, 185–190.

Morales, A.M. & Lieber, C.M. (1998). A Laser Ablation Method for the Synthesis of Crystalline Semiconductor Nanowires. *Sci.* **279**, 208–211.

Muramoto, J., Sakamoto, I., Nakata, Y., Okada, T. & Maeda, M. (1999). Influence of electric field on the behavior of Si nanoparticles generated by laser ablation. *Appl. Phys. Lett.* **75**, 751–753.

Muramoto, J., Inmaru, T., Nakata, Y., Okada, T. & Maeda, M. (2000). Spectroscopic imaging of nanoparticles in laser ablation plume by redecomposition and laser-induced fluorescence detection. *Appl. Phys. Lett.* **77**, 2334–2336.

Nakata, Y., Muramoto, J., Okada, T. & Maeda, M. (2002). Particle dynamics during nanoparticle synthesis by laser ablation in a background gas. *J. Appl. Phys.* **91**, 1640–1643.

Okamuro, K., Hashida, M., Miyasaka, Y., Ikuta, Y., Tokita, S. & Sakabe, S. (2010). Laser fluence dependence of periodic grating structures formed on metal surfaces under femtosecond laser pulse irradiation. *Phys. Rev. B.* **82**, 165417.

Phillips, A.B. & Shivaram, B.S. (2009). High capacity hydrogen absorption in transition-metal ethylene complexes: consequences of nanoclustering. *Nanotechnol.* **20**, 204020.

Renner, O., Juha, L., Krasa, J., Krousky, E., Pfeifer, M., Velyhan, A., Granja, C., Jakubek, J., Linhart, V., Slavicek, T., Vykydal, Z., Pospisil, S., Kravarik, J., Ullschmied, J., Andreev, A.A., Kampfer, T., Uschmann, I. & Forster, E. (2008). Low-energy nuclear transitions in subrelativistic laser-generated plasmas. *Laser Part. Beams* **26**, 249–257.

Roth, M., Cowan, T.E., Key, M.H., Hatchett, S.P., Brownl, C., Fountain, W., Johnson, J., Pennington, D.M., Snavely, R.A., Wilks, S.C., Yasuike, K., Ruhl, H., Pegoraro, F., Bulanov, S.V., Campbell, E.M., Perry, M.D. & Powell, H. (2001). Fast ignition by intense laser-accelerated proton beams. *Phys. Rev. Lett.* **86**, 436–439.

Schmid, M., Lenauer, C., Buchsbaum, A., Wimmer, F., Rauchbauer, G., Scheiber, P., Betz, G. & Varga, P. (2009). High Island Densities in Pulsed Laser Deposition: Causes and Implications. *Phys. Rev. Lett.* **103**, 076101.

Seto, T., Kawakami, Y., Suzuki, N., Hirasawa, M. & Aya, N. (2001). Laser Synthesis of Uniform Silicon Single Nanodots. *Nano Lett.* **1**, 315–318.

Seto, T., Orii, T., Hirasawa, M. & Aya, N. (2003). Fabrication of silicon nanostructured films by deposition of size-selected nanoparticles generated by pulsed laser ablation. *Thin Solid Films* **437**, 230–234.

Torrisi, L., Margarone, D., Laska, L., Krasa, J., Velyhan, A., Pfeifer, M., Ullschmied, J. & Ryc, L. (2008). Self-focusing effect in Au-target induced by high power pulsed laser at PALS. *Laser Part. Beams* **26**, 379–387.

Trusso, S., Barletta, E., Barreca, F., Fazio, E. & Neri, F. (2005). Time resolved imaging studies of the plasma produced by laser ablation of silicon in O_2 /Ar atmosphere. *Laser Part. Beams* **23**, 149–153.

Umezu, I., Takata, M. & Sugimura, A. (2008). Surface hydrogenation of silicon nanocrystallites during pulsed laser ablation of silicon target in hydrogen background gas. *J. Appl. Phys.* **103**, 114309.

Wang, W.T., Liu, J.S., Cai, Y., Wang, C., Liu, L., Xia, C.Q., Deng, A.H., Xu, Y., Leng, Y.X., Li, R.X. & Xu, Z.Z. (2010). Angular and energy distribution of fast electrons emitted from a solid surface irradiated by femtosecond laser pulses in various conditions. *Physics of Plasmas* **17**, 023108.

Wang, X., Yu, W., Yu, M.Y., Senecha, V.K., Xu, H., Wang, J.W., Yuan, X. & Sheng, Z.M. (2009). Efficient acceleration of a small dense plasma pellet by consecutive action of multiple short intense laser pulses. *Laser Part. Beams* **27**, 629–634.

Wang, Y.L., Li, Y.L. & Fu, G.S. (2006). Relation between size-distribution of Si nanoparticles and oscillation-stabilization time of the mixed region produced during laser ablation. *Nucl. Instr. Meth. B* **252**, 245–248.

Wang, Y.L., Xu, W., Zhou, Y., Chu, L.Z. & Fu, G.S. (2007). Influence of pulse repetition rate on the average size of silicon nanoparticles deposited by laser ablation. *Laser Part. Beams* **25**, 9–13.

Werwa, E., Seraphin, A.A., Chiu, L.A., Zhou, C. & Kolenbrander, K.D. (1994). Synthesis and processing of silicon nanocrystallites using a pulsed laser ablation supersonic expansion method. *Appl. Phys. Lett.* **64**, 1821–1823.

Yan, H., Cingarapu, S., Klabunde, K.J., Chakrabarti, A. & Sorensen, C.M. (2009). Nucleation of Gold Nanoparticle Superclusters from Solution. *Phys. Rev. Lett.* **102**, 095501.

Yogo, A., Sato, K., Nishikino, M., Mori, M., Teshima, T., Numasaki, H., Murakami, M., Demizu, Y., Akagi, S., Nagayama, S., Ogura, K., Sagisaka, A., Orimo, S., Nishiuchi, M., Pirozhkov, A.S., Ikegami, M., Tampo, M., Sakaki, H., Suzuki, M., Daito, I., Oishi, Y., Sugiyama, H., Kiriyama, H., Okada, H., Kanazawa, S., Kondo, S., Shimomura, T., Nakai, Y., Tanoue, M., Sasao, H., Wakai, D., Bolton, P.R. & Daido, H. (2009). Application of laser-accelerated protons to the demonstration of DNA double-strand breaks in human cancer cells. *Appl. Phys. Lett* **94**, 181502.

Yoshida, T., Takeyama, S., Yamada, Y. & Mutoh, K. (1996). Nanometer-sized silicon crystallites prepared by excimer laser ablation in constant pressure inert gas. *Appl. Phys. Lett.* **68**, 1772–1774.